



**HAL**  
open science

## Statistics on Jupiter's Current Sheet With Juno Data: Geometry, Magnetic Fields and Energetic Particles

Z. -Y. Liu, Q. -G. Zong, M. Blanc, Y. -X. Sun, J. -T. Zhao, Y. -X. Hao, B. H. Mauk

► **To cite this version:**

Z. -Y. Liu, Q. -G. Zong, M. Blanc, Y. -X. Sun, J. -T. Zhao, et al.. Statistics on Jupiter's Current Sheet With Juno Data: Geometry, Magnetic Fields and Energetic Particles. Journal of Geophysical Research Space Physics, 2021, 126, 10.1029/2021JA029710 . insu-03672356

**HAL Id: insu-03672356**

**<https://insu.hal.science/insu-03672356v1>**

Submitted on 24 Jun 2022

**HAL** is a multi-disciplinary open access archive for the deposit and dissemination of scientific research documents, whether they are published or not. The documents may come from teaching and research institutions in France or abroad, or from public or private research centers.

L'archive ouverte pluridisciplinaire **HAL**, est destinée au dépôt et à la diffusion de documents scientifiques de niveau recherche, publiés ou non, émanant des établissements d'enseignement et de recherche français ou étrangers, des laboratoires publics ou privés.

Copyright

# JGR Space Physics

## RESEARCH ARTICLE

10.1029/2021JA029710

### Key Points:

- The spatial distributions of current sheet magnetic fields and energetic particles are derived from Juno data
- The statistical current sheet thickness is comparable with the gyro-radius of ions that dominate the plasma pressure
- The flux of oxygen- and sulfur-group ions is comparable with the flux of protons

### Supporting Information:

Supporting Information may be found in the online version of this article.

### Correspondence to:

Q.-G. Zong,  
[qgzong@pku.edu.cn](mailto:qgzong@pku.edu.cn)

### Citation:

Liu, Z.-Y., Zong, Q.-G., Blanc, M., Sun, Y.-X., Zhao, J.-T., Hao, Y.-X., & Mauk, B. H. (2021). Statistics on Jupiter's current sheet with Juno data: Geometry, magnetic fields and energetic particles. *Journal of Geophysical Research: Space Physics*, 126, e2021JA029710. <https://doi.org/10.1029/2021JA029710>

Received 23 JUN 2021

Accepted 12 OCT 2021

## Statistics on Jupiter's Current Sheet With Juno Data: Geometry, Magnetic Fields and Energetic Particles

Z.-Y. Liu<sup>1</sup> , Q.-G. Zong<sup>1</sup> , M. Blanc<sup>2</sup> , Y.-X. Sun<sup>1</sup> , J.-T. Zhao<sup>1</sup> , Y.-X. Hao<sup>1</sup> , and B. H. Mauk<sup>3</sup> 

<sup>1</sup>Institute of Space Physics and Applied Technology, Peking University, Beijing, China, <sup>2</sup>IRAP, CNRS-Universit Paul Sabatier, Toulouse Cedex, France, <sup>3</sup>Applied Physics Laboratory, The Johns Hopkins University, Laurel, MD, USA

**Abstract** Jupiter's magnetosphere contains a current sheet of huge size near its equator. The current sheet not only mediates the global mass and energy cycles of Jupiter's magnetosphere, but also provides a site for many localized dynamic processes, such as reconnection and wave-particle interaction. To correctly evaluate its role in these processes, a statistical description of the current sheet is required. To this end, here we conduct statistics on Jupiter's current sheet, by using four-year Juno data obtained in the 20–100 Jupiter radius, 0–6 local time magnetosphere. The statistics show the thickness of the current sheet is comparable with the gyro-radius of ions dominating the plasma pressure. Magnetic fields in the current sheet decrease in power-law with increasing radial distances. At given energy, the flux of energetic electrons and protons increases with decreasing radial distances. On the other hand, at given radial distances, the flux decreases in power-law with increasing energy. The flux also varies with the distances to the current sheet center. The corresponding relationship can be described by a Gaussian function peaking at the current sheet center. In addition, the statistics show the flux of oxygen- and sulfur-group ions is comparable with the flux of protons at the same energy and radial distances, indicating the non-negligible role of heavy ions in the current sheet dynamics. From these results, a statistical model is constructed, providing us with a starting point of understanding the dynamics of the whole Jupiter's magnetosphere.

## 1. Introduction

Jupiter, the fifth planet from the sun, has the strongest intrinsic magnetic field among planets in the solar system. The interplay between this magnetic field and the solar wind results in a magnetosphere extending from the topside of Jupiter's atmosphere/ionosphere to beyond  $R \sim 100 R_J$  ( $1 R_J = \sim 71,400$  km, Jupiter radii; hereinafter,  $R$  represents the radial distance to the Jupiter) (Bagenal et al., 2007). Jupiter's magnetosphere is filled with plasma originating from various sources, including the solar wind, Jupiter's atmosphere/ionosphere, and Jupiter's moons. Among these sources, the moon Io, which supplies  $\sim 1$  ton plasma per second to the magnetosphere (e.g., Thomas et al., 2004), serves as the dominant one (e.g., Bolton et al., 2015). After entering the magnetosphere, plasma from Io (and other sources) is picked up by the magnetospheric corotating electric fields and corotates with Jupiter with a period of 9.92 hr. The corotation, in turn, induces a centrifugal force on plasma. This force tends to pull plasma radially outward against the magnetic forces, leading to the deformation of Jupiter's dipole-like magnetic fields (e.g., Hill et al., 1974). The deformation is reinforced by the plasma pressure gradient and anisotropy, which, as suggested by later observational and modeling work (e.g., Caudal, 1986; Mauk & Krimigis, 1987; Paranicas et al., 1991), even play a dominant role in balancing the magnetic forces. As a final result of the force balance, a current sheet is formed in Jupiter's middle and outer magnetosphere (Vasyliunas, 1983).

Because of Jupiter's dipole tilts ( $\sim 10^\circ$ ), Jupiter's current sheet is generally displaced from Jupiter's rotational equator (Khurana, 1992; Khurana & Schwarzl, 2005; Connerney et al., 1981). As a result of this displacement and Jupiter rotation, a spacecraft in Jupiter's magnetosphere would periodically cross the current sheet. These periodical crossings manifest as a series of magnetic field reversals in magnetic field data (e.g., Connerney et al., 1981; Khurana & Schwarzl, 2005). According to previous observations, magnetic field reversals can be detected from  $R \sim 10 R_J$  to almost the magnetopause (e.g., Connerney et al., 1981; Khurana & Schwarzl, 2005), suggesting the existence of the current sheet in the most of the equatorial regions of Jupiter's magnetosphere. Besides its huge size and notability in observations, the current sheet plays a

significant role in the dynamics of Jupiter's magnetosphere. The current sheet mediates the primary mass cycle of Jupiter's magnetosphere, the Vasyliunas cycle (Vasyliunas, 1983). In this cycle, plasma is first injected from moons into the current sheet, then temporally stored in the current sheet, and finally lost from the magnetosphere via reconnection between the last closed field lines in the current sheet. In addition to the mass cycle, the current sheet also mediates the angular momentum and energy transfer from Jupiter to the magnetosphere, which is suggested to be the dominant driver of Jupiter's magnetosphere (Hill, 2001; Hill et al., 1974; Vasyliunas, 1983). In addition to these global processes, the current sheet also provides a site for many localized energy conversion and transfer processes, such as reconnection (e.g., Russell et al., 1998; Sarkango et al., 2021; Vogt et al., 2020), wave-particle interaction (e.g., Horne et al., 2008; Saur et al., 2018), and turbulence dissipation (e.g., Saur et al., 2002).

In the light of its importance, the current sheet has been extensively studied since the Pioneer missions in the 1970s. It is found to be a hinge-shaped disk confined near the equator and extending from  $R \sim 10 R_J$  to almost the magnetopause (Khurana, 1992; Khurana & Schwarzl, 2005). The half-thickness of the current sheet is about  $3 R_J$  at  $R \sim 20 R_J$ , and decreases with increasing radial distances in general (e.g., Connerney et al., 2020). Viewed from off the equator, the current sheet magnetic field lines spiral out of their meridians, forming a sweepback configuration (Khurana & Kivelson, 1993). Magnetic fields in the current sheet have been modeled (e.g., Acuna & Ness, 1976; Connerney et al., 1981, 2018, 2020), based on which the current system (e.g., Khurana, 2001) and mass flow (e.g., Khurana & Kivelson, 1993; Vasyliunas, 1983) in the magnetosphere have been investigated. Besides, charged particles have also been investigated and modeled (but generally limited to the inner magnetosphere  $R < 30 R_J$ ) (e.g., Bridge et al., 1979; de Soria-Santacruz et al., 2016; Huscher et al., 2021; Khurana et al., 2004; Kim et al., 2020; Krupp et al., 2004; Mauk & Krimigis, 1987; Wang et al., 2021). The flux of these particles is found to decrease with increasing energy, radial distances, and the distances to the center of the current sheet. In addition to these static properties, activities including waves (e.g., Khurana & Kivelson, 1989a; Scarf et al., 1979), magnetic structures (e.g., plasmoid [e.g., Vogt, Jackman, et al., 2014]), and turbulence (e.g., Gershman et al., 2019; Saur et al., 2002; Tao et al., 2015) have also been studied.

In July of 2016, the Juno spacecraft (e.g., Bagenal et al., 2017) was successfully inserted into Jupiter orbit and became the second Jupiter orbiter. After a four-year investigation, Juno has accumulated a large data set of fields and particles that makes it possible to reveal the statistical characteristics of Jupiter's current sheet. In this paper, we conduct statistics on Jupiter's current sheet with Juno data obtained in the 20–100  $R_J$ , post-midnight (0–6 local time) magnetosphere. Characteristics of current sheet geometry, magnetic fields and energetic particles are investigated. These statistical results provide a sample empirical model of Jupiter's current sheet, with which one can easily obtain relevant parameters at a given position (please find relevant data of these distributions in Supporting Information S1). The rest of this paper is organized as follows. Section 2 describes the data set and methods. Section 3 describes the statistical results. Finally, we briefly summarize our findings in Section 4.

## 2. Materials and Methods

### 2.1. Juno Data

In this study, we use magnetic field data obtained by the Magnetometer (MAG) (Connerney et al., 2017) and energetic particle data obtained by the Juno Energetic Particle Detector Instrument (JEDI) (Mauk et al., 2017). MAG data is used to resolve the geometry and magnetic field profiles of the current sheet. The sampling time of MAG data used here,  $\sim 0.1$  s, is four orders of magnitude smaller than the time scale of typical current sheet crossings,  $\sim 10$  min. Hence, it is adequate to use MAG data for identifying the structure of the current sheet. JEDI uses solid-state detectors, thin foils and microchannel plate detectors to measure energy and angular distributions of electrons ( $\sim 25$ – $1,200$  keV), protons ( $\sim 10$ – $1,500$  keV) and heavy ions (e.g., oxygen and sulfur from  $\sim 100$  keV to  $\sim 10$  MeV). The time resolution of JEDI data used here is several seconds, small enough to resolve energetic particle profiles across the current sheet. Only look-direction averaged flux is included, although JEDI itself is capable of resolving pitch angles. Juno data used in this study is obtained during July 2016–July 2020. At the beginning and end of this time interval, the line of Juno-orbit apsides was approximately in the dawnside and midnight meridian, respectively. In other words,

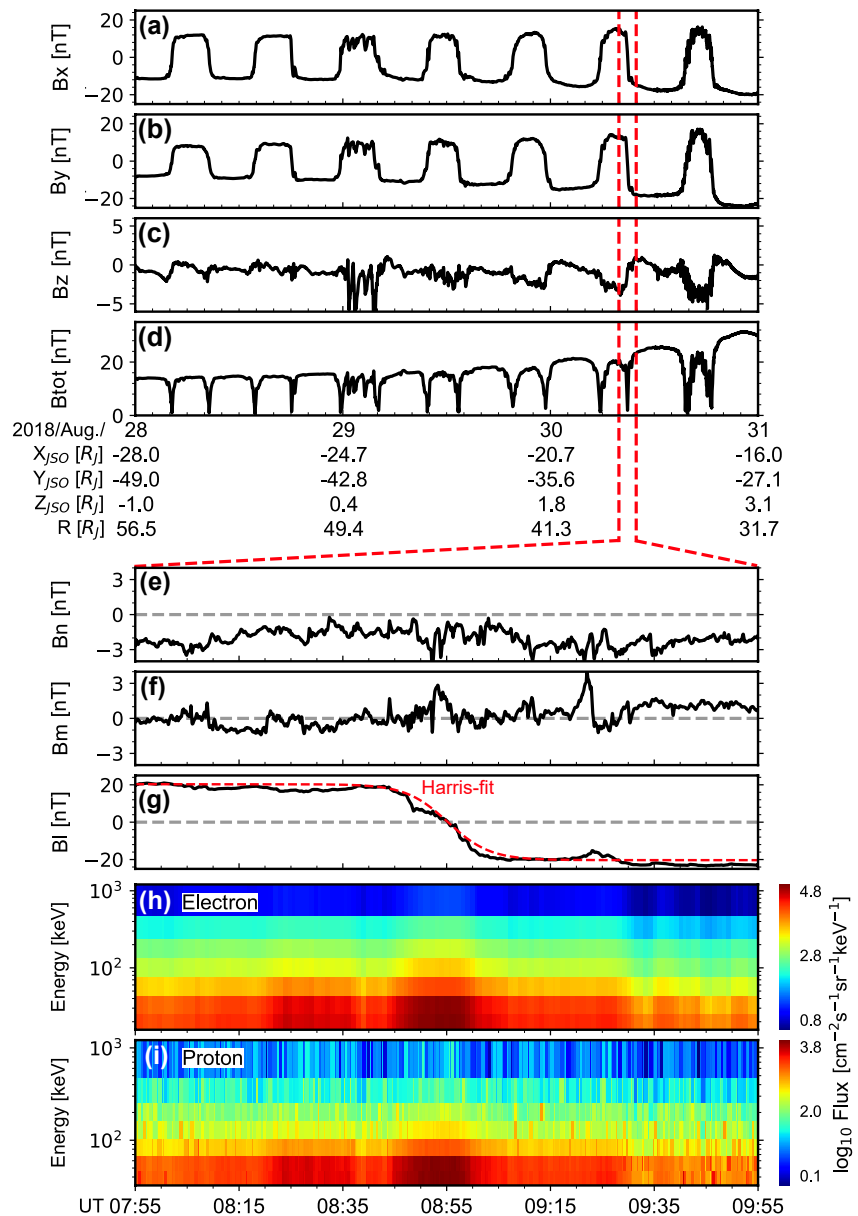


**Figure 1.** Examples of Juno current sheet crossings. (a–c) The Jupiter–Sun–Orbit (JSO) coordinate  $x$ ,  $y$ , and  $z$  components of magnetic fields. (d) The magnitude of magnetic fields. (e–g) The LMN components of magnetic fields. The red curve in (g) represents the results of the Harris fit. (h and i) The energy–time spectrograms of energetic electrons and protons during the current sheet crossing.

the data is primarily obtained in the post-midnight (0–6 local times) magnetosphere. In the following, the Jupiter–Sun–Orbit (JSO) coordinates are used, unless otherwise stated.

## 2.2. Current Sheet Crossings

As mentioned in the Introduction, Juno periodically crosses the current sheet from one hemisphere to the other, when orbiting Jupiter. Figures 1a–1d show examples of such crossings. In three days, Juno crossed the current sheet 14 times. Each crossing corresponds to a  $B_x$  and  $B_y$  reversal, and a  $B_{rot}$  decrease. The crossings appear in pairs, with one from the northern hemisphere (negative  $B_x$  and  $B_y$ ) to the southern hemisphere (positive  $B_x$  and  $B_y$ ), and the other one in the opposite order. As expected, these crossing pairs appear quasi-periodically, with a period close to Jupiter’s spin period.

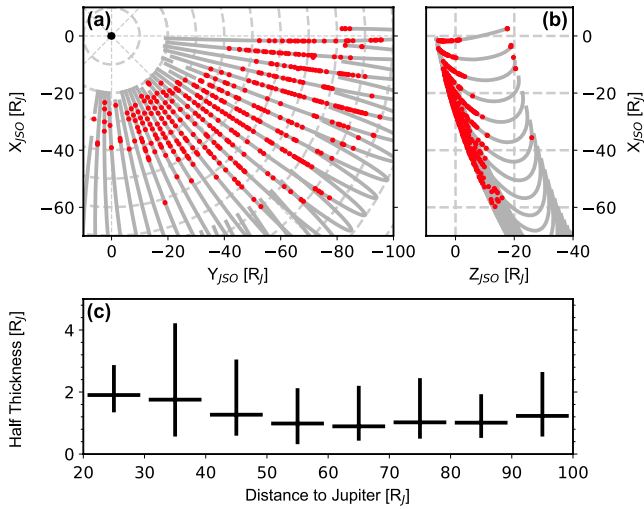


**Figure 2.** The geometry of the current sheet. (a and b) The positions of the 404 identified current sheet crossings in the Jupiter-Sun-Orbit (JSO) coordinates. The over-plotted gray curves show the trajectory of Juno. (c) The half-thickness of the current sheet. The horizontal lines correspond to the median values in each radial distance bin, while the vertical lines correspond to the error bars defined according to 25% and 75% quartiles.

We examine in greater detail one of these crossings in Figure 1 bottom. Figures 1e–1g show magnetic fields in the LMN coordinates, with L corresponding to the direction of lobe magnetic fields (increasing inward), N corresponding to the direction normal to the current sheet (increasing upward), and M completing the right-handed coordinates (increasing westward, in opposite to corotation). The LMN components are derived from the minimum variance analysis (MVA) (e.g., Sonnerup & Scheible, 1998), whose reliability is guaranteed by the relationship  $\lambda_1 : \lambda_2 : \lambda_3 \approx 100 : 10 : 1$ , where  $\lambda_1$ ,  $\lambda_2$ , and  $\lambda_3$  represent the maximum, intermediate and minimum eigenvalue of the MVA, respectively. The most notable signature of the current sheet crossing is the changes in  $B_l$ , which indicates the location of Juno relative to the current sheet. At the beginning, Juno was in the southern lobe as indicated by the positive values and plateau-like shape of  $B_l$ . Then, Juno crossed the current sheet in about 30 min, as suggested by the  $B_l$  reversal. Finally, Juno entered the northern lobe, in which  $B_l$  is negative and shows a plateau-like shape again. Accompanying the changes in  $B_l$ , the flux of energetic particles changes during the crossing. Figures 1h and 1i show the flux of energetic electrons and protons, respectively. The flux increases with decreasing  $|B_l|$ , indicating the concentration of energetic particles at the center current sheet.

To quantitatively analyze the structures of the current sheet, we apply a Harris fit to the observed current sheet crossings. Generally,  $B_l$  profiles satisfy the Harris current sheet model (Harris, 1962) that represents an equilibrium solution to the Maxwell-Vlasov equations,

$$B_l(z) = B_0 \tanh\left(\frac{z - z_0}{H}\right), \quad (1)$$

where  $B_0$  is the asymptotic lobe field,  $z_0$  corresponds to the positions of the current sheet center in N directions, and  $H$  is the characteristic half-thickness of the current sheet. Further, we note that current sheet crossings analyzed in this paper are a consequence of the corotation of the current sheet, or, equivalently, the rotation of Juno in the rest frame of Jupiter. Therefore,  $z - z_0$  can be rewritten as  $v_n(t - t_0)$ , where  $v_n$  is the N component of the corotation velocity,  $t$  is the time, and  $t_0$  is the crossing time defined by  $B_l = 0$ . With this notation, we can directly apply the Harris fit to  $B_l$  time series. The red curve in Figure 1g presents the  $B_l$  curve reconstructed from the Harris fit. It agrees well with the observations. To qualify the Harris fit, relative residual defined as  $S = \sqrt{\frac{1}{N}(B_{lf} - B_{lo})^2}/B_0$  is used, where  $N$  is the number of data points,  $B_{lf}$  and  $B_{lo}$  are the results of the fit and the observations, respectively, and  $B_0$  represents the lobe field given by the Harris model. A fit is termed as “well” when  $S < 0.2$ . With this criterion, we find most ( $\sim 90\%$ ) current sheet crossings studied in this paper match the Harris model well. In the cases for which the fit is not good, large-amplitude waves, current sheet flapping motion, or magnetic structures (e.g., plasmoid) can usually be observed.

### 2.3. Statistics

In the light of the examples shown in Figure 1, we adopt the following criteria to identify current sheet crossings: (a)  $B_x$  and  $B_y$  reverses. (b) During the 50 min before and after the reversal, a time interval of 10 min can be found, in which the standard deviation of  $B_x$  and  $B_y$  is an order

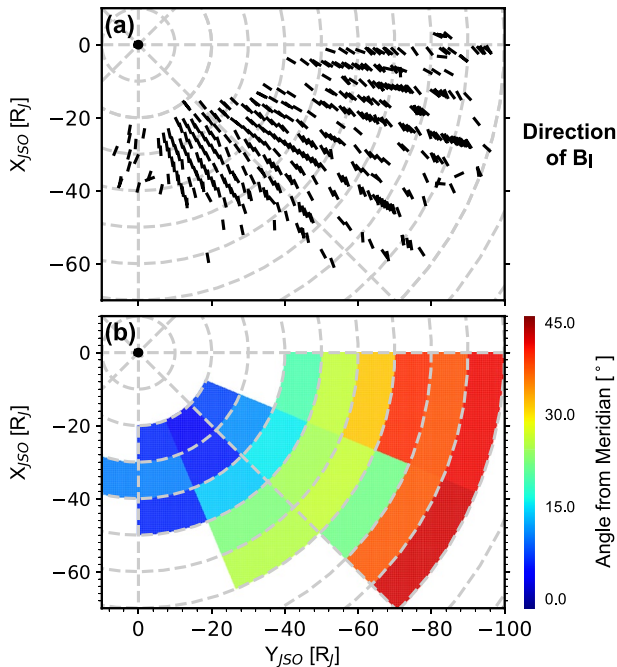


**Figure 3.** The geometry of lobe magnetic field lines. (a) The JSO (Jupiter-Sun-Orbit) equatorial plane projections of lobe magnetic fields measured in the 404 current sheet crossings. (b) The angles between the radial direction and the JSO equatorial plane projections of lobe magnetic fields. The color codes represent the medial values in each spatial bin.

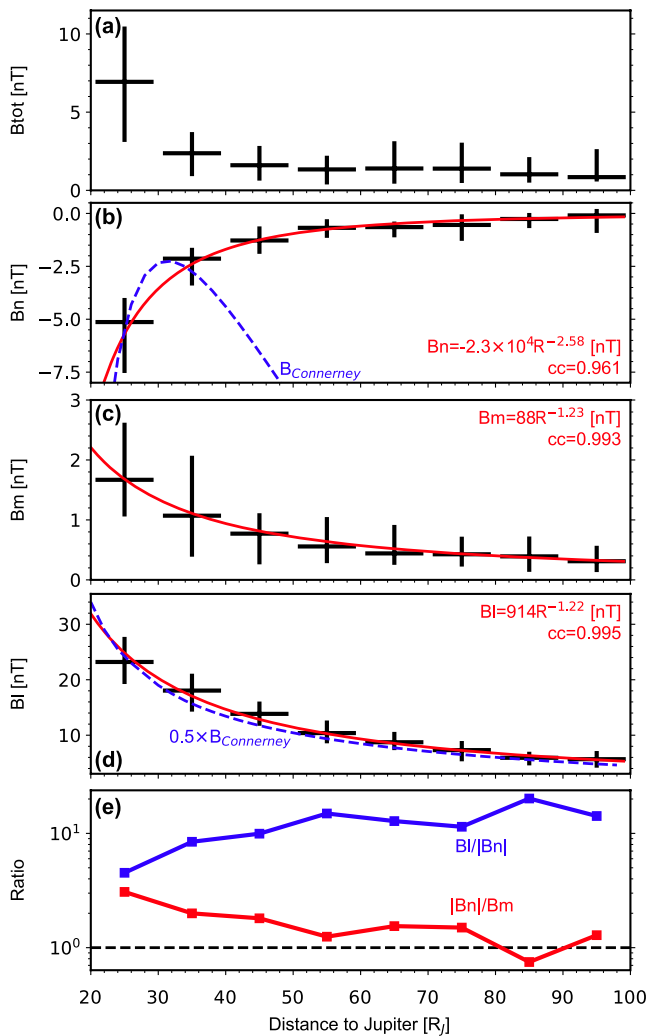


**Figure 4.** The radial distribution of magnetic fields. (a–d) The radial distributions of  $B_{iot}$ ,  $B_n$ ,  $B_m$  and  $B_i$ , respectively. The red curves represent power-law fit of the data. The blue curves correspond to the Connerney models (see text). (e) The ratio between  $B_i$  and  $|B_n|$  (blue curve), and  $|B_n|$  and  $B_m$  (red curve).

of magnitude smaller than the corresponding mean values. In addition, the mean values before and after the reversal should be opposite in sign. This criterion is proposed to distinguish current sheet crossings from large-amplitude waves and magnetic structures. In addition to the two criteria, we restrict radial distances to 20–100  $R_J$ , since inside 20  $R_J$ , the latitude of Juno is too high for it to cross the current sheet, and outside 100  $R_J$ , it is hard to distinguish current sheet crossings from large-amplitude waves and magnetic structures frequently occurring here. We note that, due to current sheet flapping, several crossings could occur in a short time interval. To rule them out and leave crossings only caused by corotation, if several crossings are identified in 2 hr, we would use the intermediate one to represent them. Based on these criteria, 404 current sheet crossings are identified.

In this paper, most statistical results are given as radial distributions, which are defined as a function of the radial distance to Jupiter. To obtain this type of distributions, we first evenly divide 20–100  $R_J$  into eight bins. Then, we classify crossings into these bins according to their radial distances. Finally, we calculate the median values of these bins, and obtain corresponding radial distributions. In the following, error bars are defined according to the 25% and 75% quartiles, if they are shown. Crossing distributions are also used to represent statistical results. For simplicity, crossing distributions are defined as a function of  $z_B = B_i/B_{i0}$ , which monotonically increases as the distance to the current sheet center increases. Here,  $B_{i0}$  represents the asymptotic lobe fields.

### 3. Results

In this section, we show the results of the statistics.

#### 3.1. Geometry

Figures 2a and 2b give the positions of the 404 current sheet crossings, together with Juno orbits shown as gray curves. Most crossings are observed around the JSO equator ( $\pm 10^\circ$  JSO latitude), although Juno also covers high latitude regions. The absence of crossings at high latitude is best illustrated by the observations in the  $R > 40R_J$ , midnight region. Because of the high latitude of Juno here, no crossings are identified in Juno data in this region, although previous studies have demonstrated

the existence of the current sheet in this region (e.g., Khurana & Schwarzl, 2005). On the other hand, we note that current sheet crossings can be observed at all radial distances and local times covered by Juno, as long as Juno is located near the equator.

Figure 2c shows the half-thickness of the current sheet estimated from the Harris fit (please find data in Table S1 in Supporting Information S1). As the radial distances increase, the half-thickness first decreases and then increases. This radial distribution gives a minimum half-thickness of  $\sim 0.9 R_J$  at  $R \sim 65 R_J$ . It is interesting to note that this radial location approximately coincides with the reconnection x-line identified by Vogt, Kivelson, et al. (2014) who studied Galileo data. This coincidence indicates a potential causal relationship between the minimum half-thickness and reconnection x-line, although we do not have any other evidence at this stage. Another notable feature is the relationship between the half-thickness and ion gyro-radius. Within the radial distances considered here, the statistical half-thickness is about 1  $R_J$ . On the other hand, previous studies (e.g., Kim et al., 2020; Mauk et al., 2004) suggest that the dominant pressure contributions in the current sheet come from heavy ions (O, S) of  $\sim 10$ –100 keV (termed as dominant ions hereinafter). As we will show in the next subsection, the magnetic field strength at the current sheet center is  $\sim 1$  nT. Thus,

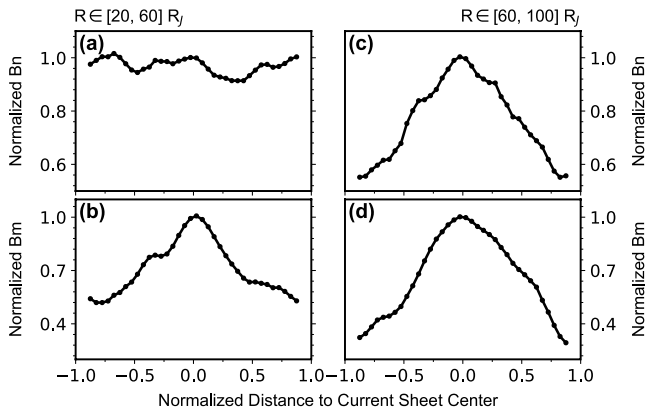


**Figure 5.** The crossing distributions of  $B_n$  and  $B_m$ . The left and right columns correspond to measurements within 20–60  $R_J$  and 60–100  $R_J$ , respectively, whereas the upper and lower rows correspond to  $B_n$  and  $B_m$ , respectively.

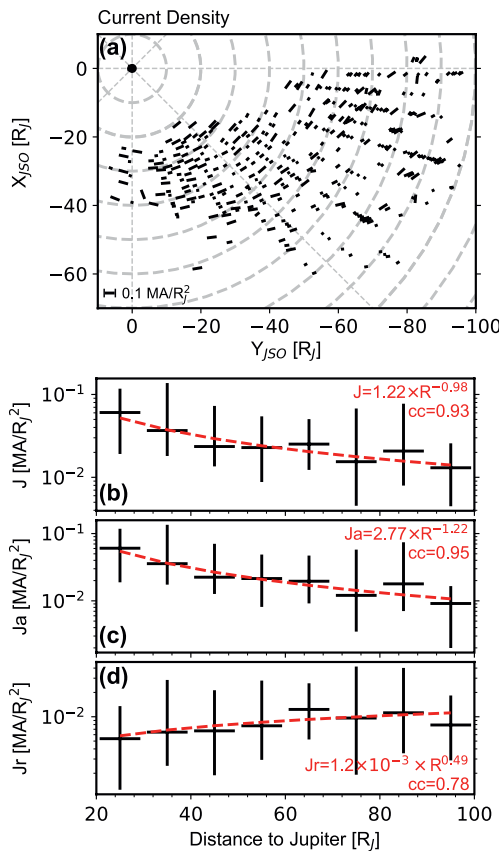


**Figure 6.** Current density at the current sheet center. (a) The JSO (Jupiter-Sun-Orbit) equatorial plane projections of the current density vectors. The length of the short lines is proportional to the magnitude of the current density. The scale is labeled at the left-bottom. (b and c) The radial distributions of total, azimuthal, and radial current density, respectively.

the gyro-radius of dominant ions in the current sheet is about  $1 R_J$ , of the same order of magnitude as the statistical half-thickness.

To understand the geometry of current sheet magnetic field lines, we plot  $B_l$  as unit vectors on the JSO equatorial plane in Figure 3a. Within  $R \sim 20\text{--}50 R_J$ ,  $B_l$  is approximately within the meridian planes. In contrast, at larger radial distances,  $B_l$  makes significant angles to the meridian planes. This feature is shown more quantitatively in Figure 3b (see Table S2 in Supporting Information S1 for data). The color code in this figure represents the median values of the angles between the JSO equatorial projection of  $B_l$  and the radial direction in each bin. It is clear that the angles gradually increase from  $0^\circ$  at  $R \sim 20 R_J$  to  $\sim 45^\circ$  at  $R \sim 100 R_J$ , showing that the magnetic field lines are increasingly bent toward the west as the radial distances increase. This observation suggests a sweepback configuration of the magnetic field lines, which has also been observed in data obtained by other spacecraft, like Voyager (Khurana & Kivelson, 1993) and Galileo (Khurana, 2001).

### 3.2. Magnetic Fields

Figure 4 shows the radial distributions of the magnetic fields. Figure 4a shows the magnitude of the magnetic fields at the current sheet center where  $B_l = 0$ . It decreases as the radial distances increase, as expected. Figure 4b gives  $B_n$  at the current sheet center. As indicated by the over-plotted red curve, this profile can be well fitted by a power-law function,

$$B_n = -2.3 \times 10^4 R^{-2.58}, \quad (2)$$

where  $R$  is radial distance in  $R_J$ , and  $B_n$  is in nT. This fit suggests a slower radial decreasing rate of  $B_n$  than a dipole field ( $R^{-3}$ ). Figure 4c shows the radial distribution of  $B_m$  at the current sheet center. This profile can be fitted by a power-law function as well,

$$B_m = 88 R^{-1.23}. \quad (3)$$

The exponent of  $B_m$ ,  $-1.23$ , is about one-half of the exponent of  $B_n$ ,  $-2.58$ . This indicates the ratio between  $|B_n|$  and  $B_m$  decreases with increasing radial distances. However, we note  $|B_n|$  is larger than  $B_m$  at almost all radial distances (Figure 4e red curve). Figure 4d presents the radial distribution of the asymptotic lobe field,  $B_l$ . This distribution satisfies the following formula,

$$B_l = 914 R^{-1.22}. \quad (4)$$

This distribution suggests the current sheet becomes more stretched at larger radial distances, since  $B_l$  decreases more slowly than  $B_n$  with increasing radial distances (Figure 4e blue curve). We note that Khurana and Kivelson (1989b) conducted a similar power-law fit on data obtained by Voyager 2 in 1979. However, they got slightly different exponents:  $-2.4$  for  $B_n$  and  $-1.54$  for  $B_l$ . At this stage, we cannot distinguish whether temporal or spatial variations cause the differences.

It would be helpful to compare the statistical distributions obtained here with magnetic field models in the literature. To this end, here we derive current sheet magnetic fields from the state-of-the-art internal model JRM09 (Connerney et al., 2018) plus the Connerney et al. (2020) current sheet model, both of which are developed from Juno/MAG measurements.

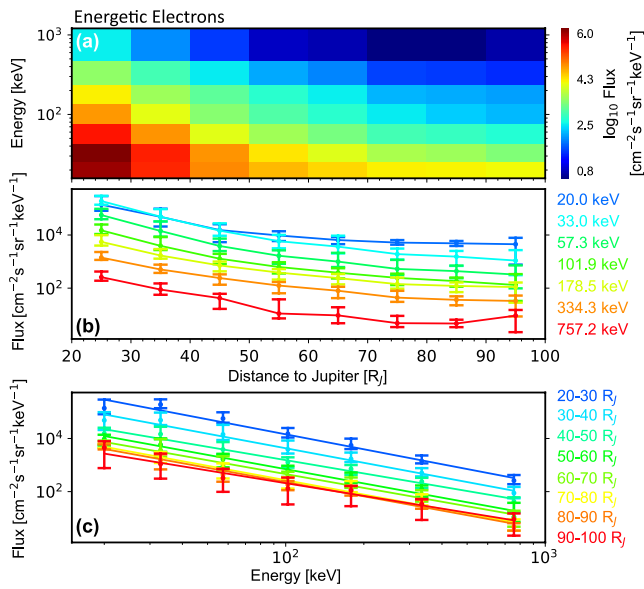


**Figure 7.** Energetic electrons. (a) The energy-radial distance spectrograms of energetic electron flux. The color codes represent the medial values in each bin. (b and c) The flux of energetic electrons as a function of radial distances and energy, respectively.

On the one hand, with a factor of 0.5, the model  $B_l$  (Figure 4d blue curve) matches the observations well in radial tendency. This good match supports the reliability of the Connerney current sheet model, since  $B_l$  not only dominates magnetic fields, but also determines the geometry of the current sheet. On the other hand, we note the model  $B_n$  (Figure 4b blue curve) significantly deviates from the observations outside  $R \sim 30 R_J$ , although it approximately matches the observations inside  $R \sim 30 R_J$ . This deviation results from the fact that the current system in Connerney et al. (2020) is restricted to radial distance  $\sim 10$ – $50 R_J$ . Consequently, at and beyond the outer edge of the current system, the magnitude of  $B_n$  at the current sheet center would increase with increasing radial distances. Global current system models are required to better model the outer current sheet.

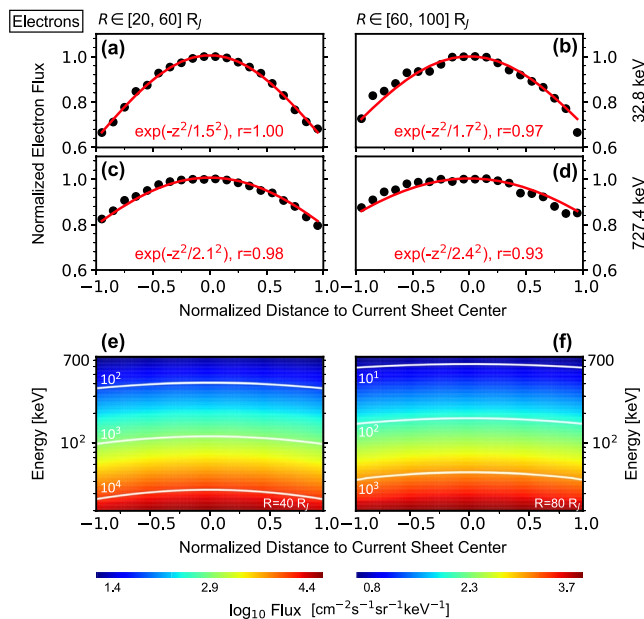
Figure 5 presents the crossing distributions of normalized  $B_n$  and  $B_m$ , with the left and right column corresponding to crossings identified within  $R \sim 20$ – $60 R_J$  and  $R \sim 60$ – $100 R_J$ , respectively. Here, the normalization is conducted by dividing  $B_n$  and  $B_m$  during a crossing by their values at  $B_l = 0$ . Generally,  $B_n$  and  $B_m$  increase toward the center current sheet. The degree of variability is higher at larger radial distances than that at smaller radial distances. For example, within  $R \sim 20$ – $60 R_J$ ,  $B_n$  does not change much across the current sheet, whereas within  $R \sim 60$ – $100 R_J$ ,  $B_n$  in the lobes is only about 60% of that at the current sheet center. Also, the degree of variability is higher for  $B_m$  than  $B_n$ . For example, within  $R \sim 60$ – $100 R_J$ ,  $B_n$  and  $B_m$  in the lobes are about 40% and 60% of  $B_n$  and  $B_m$  at the current sheet center, respectively.

### 3.3. Current Density

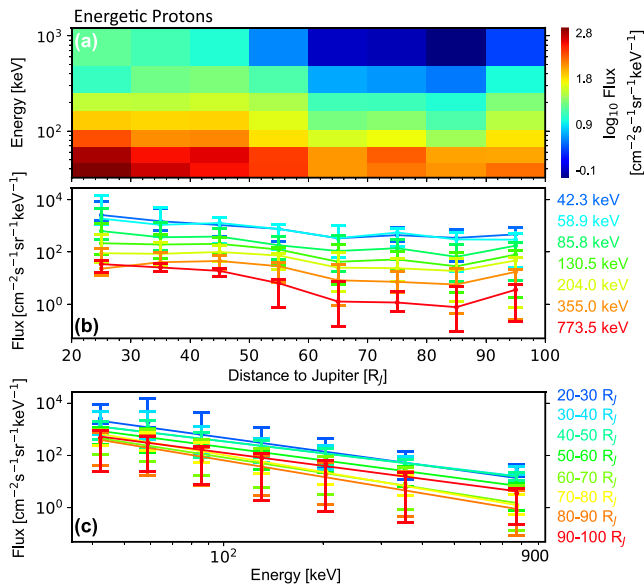
With the magnetic field and thickness observations, one can estimate the current density in the current sheet. According to the Harris model, the current density at the current sheet center is given by:  $J = (\frac{1}{\mu_0} \frac{dB_l}{dz})_{z=z_0} = \frac{B_0}{\mu_0 H}$ . In the real current sheet, the gradient of  $B_m$  would also contribute to the current density. However, as shown in Figure 4,  $B_l$  is an order of magnitude larger than  $B_m$  throughout the whole radial extent of interest. Therefore, the contributions from  $B_m$  can be neglected to a first order approximation. In the following, the current density is calculated from  $B_l$ .

Figure 6a shows the JSO equatorial plane projections of the current density vectors, with the length of the projections proportional to the magnitude of the current density. In general, the current density is larger at smaller radial distances. This dependence is shown more clearly in Figure 6b that gives the radial distribution of the current density. Approximately, the current density varies inversely with the radial distance, as shown by the power-law fit with an exponent of  $-0.98$ . The radial dependence and the order of magnitude of the current density obtained by Juno are consistent with the observations obtained by Galileo spacecraft two decades ago (Khurana, 2001).

Another feature of Figure 6a is the deviation of the current density vectors from the azimuthal direction at large radial distances. As a result, the radial current density builds up at the expense of the azimuthal current density at large radial distances. Figures 6c and 6d illustrate this phenomenon quantitatively. The azimuthal component of the current density also decreases with increasing radial distances as a power law, as the total



**Figure 8.** The crossing distributions of energetic electron flux. (a–d) Energetic electron flux at different radial distances and energies. (e and f) The reproduced energetic electron flux, with parameters determined from the statistics.



**Figure 9.** Energetic protons. (a) The energy-radial distance spectrograms of energetic proton flux. The color codes represent the medial values in each bin. (b and c) The flux of energetic protons as a function of radial distances and energy, respectively.

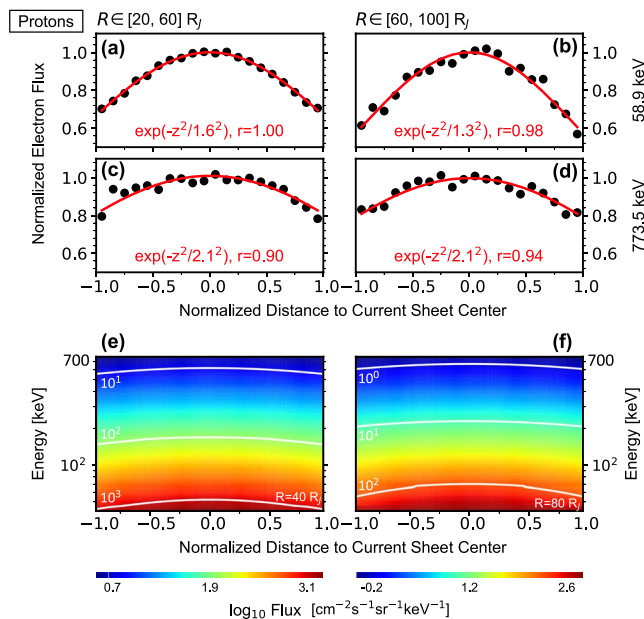


**Figure 10.** The crossing distribution of energetic proton flux. (a–d) Energetic protons flux at different radial distances and energy. (e and f) The reproduced energetic proton flux, with parameters determined from the statistics.

current density does (Figure 6b). However, the exponent,  $-1.22$ , suggests a faster decrease than the total current density. On the other hand, the radial component of the current density increases with increasing radial distances, showing the buildup of the radial current at large radial distances. We note that the radial increase of the radial current (not current density) should be more significant, since the section area  $2\pi RH$  increases with increasing radial distances.

With the distributions shown here, we can estimate the total current in the current sheet. First, we calculate the total azimuthal current in the 20–100  $R_J$  current sheet. For simplicity, here we approximate the thickness of the current sheet as 1  $R_J$  throughout the whole current sheet. Therefore, we have  $I_a = \int_{20}^{100} dR \int_{-H}^{+H} dH \frac{2.77R^{-1.22}}{\cosh^2(z/H)} \sim 3$  MA. The total azimuthal current in the current sheet is on the order of Mega-Ampere. For the radial current, we have  $I_r = 2\pi RHJ_r = 7.5 \times 10^{-3} R^{1.49}$  MA. As an example, we note the radial current at  $R \sim 50 R_J$  is  $\sim 2.5$  MA, also on the order of Mega-Ampere.

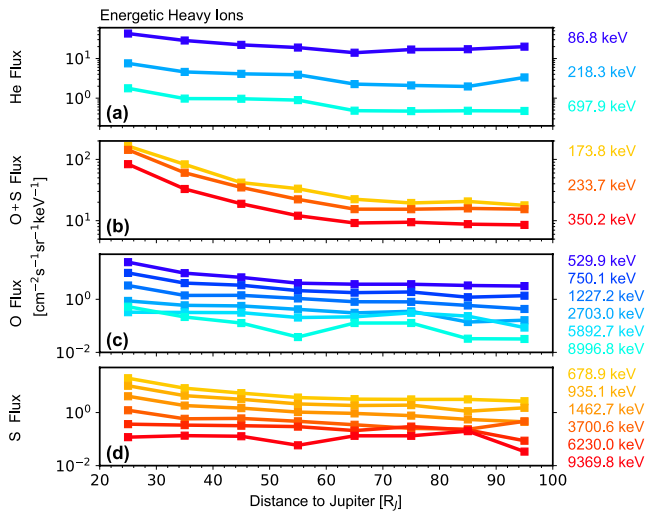
### 3.4. Energetic Electrons

Figure 7 presents the radial distributions of energetic (20–757 keV) electron flux. Figure 7a shows electron flux as a function of radial distance and energy (Table S3 in Supporting Information S1). In general, electron flux increases with decreasing radial distances and energy. Figure 7b illustrates the radial variations more clearly. Not only does electron flux decrease with increasing radial distances, but also the maximum/minimum flux ratios decrease as energy increase. As shown, the ratio between flux at  $R \sim 20 R_J$  and  $R \sim 100 R_J$  is about 100 and 50 for energy below and above 100 keV, respectively. Figure 7c shows the energy spectra of electrons at different radial distances. As indicated by the over-plotted lines, these spectra can be well fitted by power laws. The exponents of these power laws are about 2, and slightly decrease with increasing radial distances.

Figure 8 illustrates how electron flux varies across the current sheet. Figures 8a–8d show the crossing distributions of electron normalized flux, with the left and right column representing flux within  $R \sim 20$ – $60 R_J$  and  $R \sim 60$ – $100 R_J$ , respectively, and the upper and lower row corresponding to 33 and 724 keV, respectively. The normalization performed here is the same as the one conducted in Figure 5. It is clear that all crossing distributions can be fitted by Gaussian functions,  $\exp(-z_B^2/\sigma^2)$ . The fit parameter  $\sigma$ , which represents the width of the distribution, generally increases with increasing radial distances and energy (Table S4 in Supporting Information S1). This indicates a relatively lower lobe electron flux at smaller radial distances and lower energy. The crossing distributions shown here, together with the radial and energy distributions shown in Figure 7, give a statistical model of energetic electron flux (see Text S1 in Supporting Information S1 for detailed information). As an example, Figures 8e and 8f show electron flux reproduced from this model.

### 3.5. Energetic Ions

Figure 9 shows the radial distributions of energetic proton flux, with the same format as Figure 7 (Table S5 in Supporting Information S1).



**Figure 11.** The flux of energetic heavy ions, with (a) to (d) corresponding to alpha, O + S, O, and S, respectively.

Similarities can be found between proton and electron distributions. First, in the most radial extent covered by Juno, proton flux decreases as the radial distances increase, the same as electron flux does. Second, at fixed radial distances, the energy spectra of protons can be fitted by power laws. The exponents of these power laws are about two and decrease slightly with increasing radial distances. Despite these similarities, there are also significant differences. First, the radial dependence is weaker for protons than electrons, as the ratio between flux at  $R \sim 20 R_J$  and  $R \sim 100 R_J$  is  $<10$  for protons and  $>50$  for electrons. Second, at the far-end of the radial distributions, proton flux increases rather than decreases with increasing radial distances. Actually, the same is also seen for electrons of the highest energy channel. Currently, we do not have any solid explanation for this. Third, at fixed radial distances and energy, the statistical errors are larger for proton flux than electron flux, as shown by the error bars in Figures 7c and 9c. Since these errors primarily arise from temporal variations, these results indicate a stronger temporal variability for proton flux than electron flux.

Figure 10 gives the crossing distributions of proton flux, with the same format as Figure 8. As illustrated by Figures 10a–10d, proton flux can also be fitted by Gaussian functions (Table S5 in Supporting Information S1).

The fit parameter of proton distributions is close to that of electron distributions.

In a similar way to what we did for electrons, the statistical radial, energy, and crossing distributions shown here provide a model of energetic proton flux. Flux reproduced from this model is shown in Figures 10e and 10f.

Besides protons, we also conduct statistics on energetic heavy ions. From top to bottom, Figure 11 shows the statistical flux distributions of alpha particles, O + S, O, and S (Table S6 in Supporting Information S1). Heavy ion flux also decreases as the radial distances increase. However, it decreases faster than proton flux does. For example, the fluxes of O + S at  $R \sim 20 R_J$  is  $\sim 100$  times larger than that at  $R \sim 100 R_J$ , whereas for protons, the corresponding ratio is  $<10$ . Another notable feature of Figure 11 is that, at the same energy and radial distances, the flux of oxygen and sulfur ions are comparable with that of  $H^+$ . This result agrees with observations obtained by other spacecraft missions. For example, from the Galileo data, Mauk et al. (2004) concluded that the flux of 50 keV–50 MeV heavy ions (O, S) is comparable to or even greater than that of protons. All these results indicate the effects of heavy ions on the dynamics of Jupiter’s current sheet are non-negligible.

It would be helpful to compare the results obtained here with that of Kim et al. (2020) (their Figure 7), who investigated the density and temperature of the plasma in the 10–50  $R_J$  current sheet based on Juno/JADE-I data of  $<50$  keV ions. In the radial extent overlapped by both studies (20–50  $R_J$ ), the number density of core ( $<50$  keV)  $H^+$  is  $\sim 10^{-2}$   $\text{cm}^{-3}$ , while the partial number density of energetic ( $>50$  keV)  $H^+$ , which is obtained by first converting JEDI flux into phase space densities (PSDs) (Roederer & Zhang, 2016) and then integrating the PSDs over all JEDI energy channels, is  $\sim 10^{-3}$   $\text{cm}^{-3}$ . Therefore, the energetic  $H^+$  contribute  $\sim 10\%$  to the total  $H^+$  number density. On the other hand, the temperature of core  $H^+$  is  $\sim 10$  keV, corresponding to an energy density of 0.1 keV/ $\text{cm}^3$ . Based on JEDI data, we find the energy density of energetic  $H^+$  is  $\sim 0.3$  keV/ $\text{cm}^3$  (The contribution from corotation,  $\sim 10^{-3}$  keV/ $\text{cm}^3$ , is negligible even at  $R \sim 50 R_J$  and under the rigid corotation assumption). Thus, energetic  $H^+$  contribute more to the total plasma energy density than core  $H^+$  do. In addition, we note that Kim et al. (2020) found the number density of core O and S ions ( $\sim 10^{-2}$   $\text{cm}^{-3}$ ) is of the same order of magnitude as  $H^+$ , as is the energetic ion case.

#### 4. Summary

In this paper, we conducted statistics on Jupiter’s current sheet, based on four-year Juno observations obtained in the 20–100  $R_J$ , post-midnight (0–6 local time) magnetosphere.

The main results of the statistics are summarized as follows:

1. Within  $R \sim 20\text{--}100 R_J$ , the statistical half-thickness of the current sheet is comparable with the gyro-radius of ions dominating the plasma pressure ( $\sim 10\text{--}100$  keV heavy ions, e.g., O and S).
2. As the radial distances increase from  $R \sim 20 R_J$  to  $100 R_J$ , the angles between lobe magnetic fields and the radial direction increase from  $0^\circ$  to  $45^\circ$ , indicating a sweepback configuration of the magnetic field lines in the current sheet.
3. The radial distribution of  $B_n$ ,  $B_m$  and  $B_l$  can be well fitted by power laws, with corresponding exponents of  $-2.58$ ,  $-1.23$ , and  $-1.22$ , respectively. These exponents indicate a more stretched configuration at larger radial distances, as  $B_l/|B_n|$  increases with increasing radial distances.
4. In general,  $B_n$  and  $B_m$  increase as the distances to the current sheet center decreases.
5. As the radial distances increase, the radial current density increases, while the azimuthal current density decreases. Integrated over space, the total current in Jupiter's current sheet is on the order of a few Mega-Amperes.
6. The flux of energetic electrons and ions increases as energy, radial distances, and the distances to the current sheet center decrease.
7. The energy spectra of energetic electrons and protons can be fitted by power laws. The corresponding exponents are  $\sim 2$  for both electrons and protons.
8. At the same energy and radial distances, the flux of oxygen-group ions and sulfur-group ions is comparable with the flux of protons.

These statistical results provide a basic description of Jupiter's current sheet. They can be used in numerical simulations as initial inputs or background, and also for the design of future Jupiter missions.

## Data Availability Statement

The statistical data set is included in Supporting Information S1, and is published on Zenodo (<https://doi.org/10.5281/zenodo.5553567>).

## Acknowledgments

This work was supported by the China Space Agency project (D020301) and the National Natural Science Foundation of China (42011530080). Michel Blanc wishes to express his gratitude to CNES for its support to his participation in the Juno mission. The authors are very grateful to NASA and to the contributing institutions that have made the Juno mission possible, and to all institutions supporting the development, operation and data analysis of the Juno instruments used in this study: MAG and JEDI. Our special thanks to Dr. John E. Connerney, Principal Investigator of the MAG experiment and to the MAG team for providing data critical to this study. The authors acknowledge the use of NASA Planetary Plasma Interactions Node for obtaining Juno data, including the MAG data (<https://pds-ppi.igpp.ucla.edu/search/view/?f=yes&id=pds://PPI/JNO-J-3-FGM-CAL-V1.0/DATA>) and the JEDI data (<https://pds-ppi.igpp.ucla.edu/search/view/?f=yes&id=pds://PPI/JNO-J-JED-3-CDR-V1.0/DATA>).

## References

- Acuna, M. H., & Ness, N. F. (1976). The main magnetic field of Jupiter. *Journal of Geophysical Research*, *81*(16), 2917–2922. <https://doi.org/10.1029/ja081i016p02917>
- Bagenal, F., Adriani, A., Allegrini, F., Bolton, S., Bonfond, B., Bunce, E., et al. (2017). Magnetospheric science objectives of the Juno mission. *Space Science Reviews*, *213*(1), 219–287. <https://doi.org/10.1007/s11214-014-0036-8>
- Bagenal, F., Dowling, T. E., & McKinnon, W. B. (2007). *Jupiter: The Planet, Satellites and Magnetosphere* (Vol. 1). Cambridge University Press.
- Bolton, S. J., Bagenal, F., Blanc, M., Cassidy, T., Chané, E., Jackman, C., et al. (2015). Jupiter's magnetosphere: Plasma sources and transport. *Space Science Reviews*, *192*(1), 209–236. <https://doi.org/10.1007/s11214-015-0184-5>
- Bridge, H., Belcher, J., Lazarus, A., Sullivan, J., McNutt, R., Bagenal, F., et al. (1979). Plasma observations near Jupiter: Initial results from voyager 1. *Science*, *204*(4396), 987–991. <https://doi.org/10.1126/science.204.4396.987>
- Caudal, G. (1986). A self-consistent model of Jupiter's magnetodisc including the effects of centrifugal force and pressure. *Journal of Geophysical Research*, *91*(A4), 4201–4221. <https://doi.org/10.1029/ja091ia04p04201>
- Connerney, J., Acuna, M., & Ness, N. (1981). Modeling the Jovian current sheet and inner magnetosphere. *Journal of Geophysical Research*, *86*(A10), 8370–8384. <https://doi.org/10.1029/ja086ia10p08370>
- Connerney, J., Benn, M., Bjarno, J., Denver, T., Espley, J., Jorgensen, J., et al. (2017). The Juno magnetic field investigation. *Space Science Reviews*, *213*(1), 39–138. <https://doi.org/10.1007/s11214-017-0334-z>
- Connerney, J., Kotsiaros, S., Oliverson, R., Espley, J., Joergensen, J. L., Joergensen, P., et al. (2018). A new model of Jupiter's magnetic field from Juno's first nine orbits. *Geophysical Research Letters*, *45*(6), 2590–2596. <https://doi.org/10.1002/2018gl077312>
- Connerney, J., Timmins, S., Herceg, M., & Joergensen, J. (2020). A Jovian magnetodisc model for the Juno era. *Journal of Geophysical Research: Space Physics*, *125*(10), e2020JA028138. <https://doi.org/10.1029/2020ja028138>
- de Soria-Santacruz, M., Garrett, H., Evans, R., Jun, I., Kim, W., Paranicas, C., & Drozdov, A. (2016). An empirical model of the high-energy electron environment at Jupiter. *Journal of Geophysical Research: Space Physics*, *121*(10), 9732–9743. <https://doi.org/10.1002/2016JA023059>
- Gershman, D. J., Connerney, J. E., Kotsiaros, S., DiBaccio, G. A., Martos, Y. M., Viñas, A. F., et al. (2019). Alfvénic fluctuations associated with Jupiter's auroral emissions. *Geophysical Research Letters*, *46*(13), 7157–7165. <https://doi.org/10.1029/2019gl082951>
- Harris, E. G. (1962). On a plasma sheath separating regions of oppositely directed magnetic field. *Nuovo Cimento*, *23*(1), 115–121. <https://doi.org/10.1007/bf02733547>
- Hill, T. (2001). The Jovian auroral oval. *Journal of Geophysical Research*, *106*(A5), 8101–8107. <https://doi.org/10.1029/2000ja000302>
- Hill, T., Dessler, A., & Michel, F. (1974). Configuration of the Jovian magnetosphere. *Geophysical Research Letters*, *1*(1), 3–6. <https://doi.org/10.1029/gl001i001p00003>
- Horne, R. B., Thorne, R. M., Glauert, S. A., Menietti, J. D., Shprits, Y. Y., & Gurnett, D. A. (2008). Gyro-resonant electron acceleration at Jupiter. *Nature Physics*, *4*(4), 301–304. <https://doi.org/10.1038/nphys897>

- Huscher, E., Bagenal, F., Wilson, R., Allegrini, F., Ebert, R., Valek, P., et al. (2021). Survey of Juno observations in Jupiter's plasma disk Density. *Journal of Geophysical Research: Space Physics*, e2021JA029446. <https://doi.org/10.1029/2021ja029446>
- Khurana, K. K. (1992). A generalized hinged-magnetodisc model of Jupiter's nightside current sheet. *Journal of Geophysical Research: Space Physics*, 97(A5), 6269–6276. <https://doi.org/10.1029/92ja00169>
- Khurana, K. K. (2001). Influence of solar wind on Jupiter's magnetosphere deduced from currents in the equatorial plane. *Journal of Geophysical Research*, 106(A11), 25999–26016. <https://doi.org/10.1029/2000ja000352>
- Khurana, K. K., & Kivelson, M. G. (1989a). On Jovian plasma sheet structure. *Journal of Geophysical Research*, 94(A911), 11791–11803. <https://doi.org/10.1029/ja094ia09p11791>
- Khurana, K. K., & Kivelson, M. G. (1989b). Ultralow frequency MHD waves in Jupiter's middle magnetosphere. *Journal of Geophysical Research*, 94(A5), 5241–5254. <https://doi.org/10.1029/ja094ia05p05241>
- Khurana, K. K., & Kivelson, M. G. (1993). Inference of the angular velocity of plasma in the Jovian magnetosphere from the sweepback of magnetic field. *Journal of Geophysical Research*, 98(A1), 67–79. <https://doi.org/10.1029/92ja01890>
- Khurana, K. K., Kivelson, M. G., Vasyliunas, V. M., Krupp, N., Woch, J., Lagg, A., et al. (2004). The configuration of Jupiter's magnetosphere. *Jupiter: The planet, satellites and magnetosphere*, 1, 593–616.
- Khurana, K. K., & Schwarzl, H. K. (2005). Global structure of Jupiter's magnetospheric current sheet. *Journal of Geophysical Research*, 110(A7). <https://doi.org/10.1029/2004ja010757>
- Kim, T. K., Ebert, R., Valek, P., Allegrini, F., McComas, D., Bagenal, F., et al. (2020). Survey of ion properties in Jupiter's plasma sheet: Juno Jade-I observations. *Journal of Geophysical Research: Space Physics*, 125(4), e2019JA027696. <https://doi.org/10.1029/2019ja027696>
- Krupp, N., Vasyliunas, V., Woch, J., Lagg, A., Khurana, K., Kivelson, M., et al. (2004). Dynamics of the Jovian magnetosphere. *Jupiter: The Planet, Satellites and Magnetosphere*, 1, 617–638.
- Mauk, B., Haggerty, D., Jaskulek, S., Schlemm, C., Brown, L., Cooper, S., et al. (2017). The Jupiter energetic particle detector instrument (JEDI) investigation for the Juno mission. *Space Science Reviews*, 213(1), 289–346. <https://doi.org/10.1007/s11214-013-0025-3>
- Mauk, B., & Krimigis, S. (1987). Radial force balance within Jupiter's dayside magnetosphere. *Journal of Geophysical Research*, 92(A9), 9931–9941. <https://doi.org/10.1029/ja092ia09p09931>
- Mauk, B., Mitchell, D., McEntire, R., Paranicas, C., Roelof, E., Williams, D., et al. (2004). Energetic ion characteristics and neutral gas interactions in Jupiter's magnetosphere. *Journal of Geophysical Research*, 109(A9). <https://doi.org/10.1029/2003ja010270>
- Paranicas, C., Mauk, B., & Krimigis, S. (1991). Pressure anisotropy and radial stress balance in the Jovian neutral sheet. *Journal of Geophysical Research*, 96(A12), 21135–21140. <https://doi.org/10.1029/91ja01647>
- Roederer, J. G., & Zhang, H. (2016). *Dynamics of magnetically trapped particles*. Springer.
- Russell, C., Khurana, K., Huddleston, D., & Kivelson, M. (1998). Localized reconnection in the near Jovian magnetotail. *Science*, 280(5366), 1061–1064. <https://doi.org/10.1126/science.280.5366.1061>
- Sarkango, Y., Slavin, J. A., Jia, X., DiBraccio, G. A., Gershman, D. J., Connerney, J. E., et al. (2021). Juno observations of ion-inertial scale flux ropes in the Jovian magnetotail. *Geophysical Research Letters*, 48(2), e2020GL089721. <https://doi.org/10.1029/2020gl089721>
- Saur, J., Janser, S., Schreiner, A., Clark, G., Mauk, B. H., Kollmann, P., et al. (2018). Wave-particle interaction of Alfvén waves in Jupiter's magnetosphere: Auroral and magnetospheric particle acceleration. *Journal of Geophysical Research: Space Physics*, 123(11), 9560–9573. <https://doi.org/10.1029/2018ja025948>
- Saur, J., Politano, H., Pouquet, A., & Matthaeus, W. (2002). Evidence for weak MHD turbulence in the middle magnetosphere of Jupiter. *Astronomy & Astrophysics*, 386(2), 699–708. <https://doi.org/10.1051/0004-6361:20020305>
- Scarf, F. L., Gurnett, D. A., & Kurth, W. S. (1979). Jupiter plasma wave observations: An initial voyager 1 overview. *Science*, 204(4396), 991–995. <https://doi.org/10.1126/science.204.4396.991>
- Sonnerup, B. U., & Scheible, M. (1998). Minimum and maximum variance analysis. *Analysis methods for multi-spacecraft data*, 1, 185–220.
- Tao, C., Sahraoui, F., Fontaine, D., de Patoul, J., Chust, T., Kasahara, S., & Retino, A. (2015). Properties of Jupiter's magnetospheric turbulence observed by the Galileo spacecraft. *Journal of Geophysical Research: Space Physics*, 120(4), 2477–2493. <https://doi.org/10.1002/2014ja020749>
- Thomas, N., Bagenal, F., Hill, T., & Wilson, J. (2004). The Io neutral clouds and plasma torus. *Jupiter: The planet, satellites and magnetosphere*, 1, 561–591.
- Vasyliunas, V. M. (1983). Plasma distribution and flow. In *Physics of the Jovian magnetosphere* (pp. 395–453). <https://doi.org/10.1017/cbo9780511564574.013>
- Vogt, M. F., Connerney, J. E., DiBraccio, G. A., Wilson, R. J., Thomsen, M. F., Ebert, R. W., et al. (2020). Magnetotail reconnection at Jupiter: A survey of Juno magnetic field observations. *Journal of Geophysical Research: Space Physics*, 125(3), e2019JA027486. <https://doi.org/10.1029/2019ja027486>
- Vogt, M. F., Jackman, C. M., Slavin, J. A., Bunce, E. J., Cowley, S. W., Kivelson, M. G., & Khurana, K. K. (2014). Structure and statistical properties of plasmoids in Jupiter's magnetotail. *Journal of Geophysical Research: Space Physics*, 119(2), 821–843. <https://doi.org/10.1002/2013ja019393>
- Vogt, M. F., Kivelson, M. G., Khurana, K. K., Joy, S. P., & Walker, R. J. (2014). SReconnection and flows in the Jovian magnetotail as inferred from magnetometer observations. *Journal of Geophysical Research: Space Physics*, 115(A6). <https://doi.org/10.1029/2009JA015098>
- Wang, J.-Z., Ma, J.-N., Huo, Z.-X., Xiong, Y., & Tian, D. (2021). Statistical study of energetic electrons in Jupiter's inner magnetosphere by Juno/JEDI. *Advances in Space Research*, 67(5), 1709–1720. <https://doi.org/10.1016/j.asr.2020.11.032>